Thin–Walled Structures 208 (2025) 112761

Contents lists available at ScienceDirect

Thin-Walled Structures

journal homepage: www.elsevier.com/locate/tws

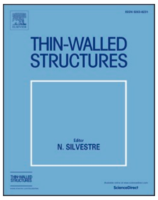

Multi-objective and multi-constraint topology optimization of nonlinear compliant mechanisms

Yifu Lu [*], Quantian Luo, Liyong Tong [*]

School of Aerospace, Mechanical and Mechatronic Engineering, The University of Sydney, Sydney, NSW 2006, Australia

ARTICLE INFO

Keywords:
Multi-objective
Multi-constraint
Compliant mechanism
Nonlinearity
Topology optimization
Finite element analysis

ABSTRACT

This study investigates multi-objective and multi-constraint design optimization of compliant mechanisms considering geometrical and material nonlinearities. When geometrical and material nonlinearities arise in optimization due to high loading levels and/or weak region/hinges, the nonlinear finite element analysis data in all load increments should be used to capture nonlinear behaviors of compliant mechanisms. Thus, in this work, we present (1) a new formulation for output displacement in terms of mutual strain energy density calculated using all incremental load steps in nonlinear finite element analysis; (2) problem formulation with multi-objective functions defined in terms of nonlinear output displacements and compliance-related displacements; and (3) an effective extended moving isosurface threshold algorithm for topology optimization of multi-objective nonlinear compliant mechanisms with displacement, buckling, and volume constraints. Numerical results for selected compliant mechanisms are presented and compared with those available in the literature to validate the present formulations and algorithm. The present results illustrate the effects of utilizing all load step nonlinear finite element analysis results on the optimum topology.

Introduction

Compliant mechanisms have attracted great research interests due to its less friction, precise and smooth movement, and cost-effectiveness in manufacturing and maintenance, while the topology design could be challenging. The simplest design is a single-input-single-output (SISO) compliant mechanism with linear deformation; topology optimization for the single-output mechanism has been extensively studied [1–5]. In practice, compliant mechanisms with multiple output ports are common in micro-electromechanical systems (MEMS) and have recently attracted considerable interests [6–9]. One of the main objectives for the optimal design of compliant mechanisms is to maximize the displacement(s) at the output port(s), and thus large deformation can be achieved. Optimization for SISO compliant mechanisms with geometrical nonlinearity has also been studied by many researchers [10–17]. As thin components and hinges often appear in the optimum compliant mechanism, material nonlinearity has been considered in [10,11,16,18–20]. Up to now, there are few attempts for topology optimization for multi-objective compliant mechanisms with multiple constraints considering geometrical and material nonlinearities.

In topology optimization for structures with geometrical nonlinearity [21–23], stiffness designs have been vastly studied in engineering applications such as composite structures [24,25], in which material and/or load nonlinearities are also considered [26–29]. In both stiffness/compliance and compliant mechanism optimization problems, stresses and strains in a final load step in nonlinear finite element analysis (NFEA) are usually used in estimating objective functions, such as the end compliance for stiffness optimization or the mutual strain energy in the final load step for compliant mechanism design [10,11,18,19,21]. Although it is simple to calculate the objective function using data in the final load step, the drawbacks are [21,22]: 1) the structure may collapse when the applied load is lower than the prescribed level; 2) it may result in a degenerated structure supporting the designed load only. When material and geometrical nonlinearities are considered in the optimization for compliant mechanism with multi-output ports, the challenges are: 1) cost associated with conducting nonlinear structural analysis for each virtual force at each output port; 2) load histories of the virtual and real forces need to be considered to find displacements at the final load state at output port; and 3) magnitude of each virtual load needs to be carefully determined as nonlinear finite element analysis can diverge for too high load and nonlinear effects cannot be reflected at very low load. Therefore, loading history should be considered in

---

[*] Corresponding authors.
E-mail addresses: yifu.lu@sydney.edu.au (Y. Lu), liyong.tong@sydney.edu.au (L. Tong).

https://doi.org/10.1016/j.tws.2024.112761
Received 16 September 2024; Received in revised form 18 November 2024; Accepted 26 November 2024

calculating objective and constraint functions for the optimization of compliant mechanisms with geometrical and material nonlinearities.

In addition to the stress constraints [30,31], displacement constraints are another common consideration in structural topology optimization. For example, the minimum mean compliance problem was studied in [32–34], and the design of compliant mechanisms with input displacement constraint was considered in [22,35]. In compliant mechanisms with multi-output ports, displacements at some ports may be constrained by application conditions [36]. In this case, the displacement constraint needs to be considered.

The moving isosurface threshold (MIST) method [37], which uses a physical response function surface and an isosurface threshold to generate the optimal topologies, has been applied to a range of topology optimization tasks, e.g., multiscale [38–40], piezoelectric [41], or vibrating structures [42]. Recently, it has become more powerful, as challenging optimization problems and advanced optimization methods, such as cloaking metamaterials [43], isogeometric topology optimization (ITO) [44], and reliability-based topology optimization (RBTO) [45], have been investigated. However, the existing MIST method can not deal with multi-objective and multi-constraint topology optimization for nonlinear structures. This work aims to extend the MIST method to solve this challenge.

In this paper, multi-objective optimization with multi-constraints is studied to maximize multi-output displacements for compliant mechanisms with geometrical and material nonlinearities. Novel displacement formulations are derived using data of every incremental load step in NFEA. An algorithm is developed based on the MIST for the proposed multi-objective and multi-constraint optimization problem to design nonlinear compliant mechanisms. Numerical results are presented for designing linear and nonlinear compliant mechanisms with single-output and two-output ports and under volume and displacement constraints.

2. Problem statement

Consider an elastic body Ω of Fig. 1 subjected to a real load $\boldsymbol{F}^{(2)}$, which has N_i components $F_{im}^{(2)}$ $(m = 1, 2, \ldots, N_i)$ applied at N_i input ports or degrees of freedom (DOFs) respectively. The problem is stated as: to find the optimum distribution or topology of a given amount of material in Ω that maximizes the displacements $u_{ol}^{(2)}$ $(l = 1, 2, \ldots, N_o)$ at N_o interested output ports or DOFs under the given load or minimizes $-u_{ol}^{(2)}$ $(l = 1, 2, \ldots, N_o)$ as shown in Fig. 1, where the superscripts (1) and (2) denote the virtual and real load cases, respectively. This problem is referred to as topology optimization of nonlinear compliant mechanisms with multi-inputs and multi-outputs (MIMO) when geometrical and/or material nonlinearities are taken into account in nonlinear finite element analysis (NFEA).

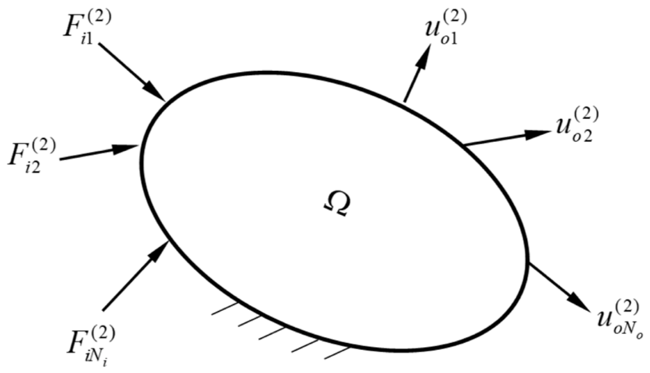

Fig. 1. Design of nonlinear compliant mechanism with multiple inputs and outputs.

2.1. Displacement formulation

As displacement at an output port is usually chosen as the objective function in topology designs of compliant mechanisms, it is important to derive the formulation of this output displacement. Such an output displacement can be expressed in terms of total mutual strain energy for linear case [46]; it can be approximated as the total mutual strain energy at the final load level for nonlinear cases [10,11]. In this section, we propose an expression for such displacement in terms of the mutual strain energy calculated using all incremental load steps.

In nonlinear analysis, an easy way is to describe loading as a function of time, and the principle of virtual work can be expressed as [47]:

$$\int_{{}^{0}\Omega} {}^{(t+\Delta t)}S_{ij}\delta\varepsilon_{ij}d^{0}\Omega = \int_{{}^{0}\Omega} {}^{(t+\Delta t)}f_i^b\delta u_i d^{0}\Omega + \int_{{}^{0}S} {}^{(t+\Delta t)}f_i^s\delta u_i d^{0}S + {}^{(t+\Delta t)}f_i^c\delta u_i \tag{1a}$$

where S_{ij} and ε_{ij} denote the second Piola-Kirchhoff stress and Green-Lagrange strain tensors; f_i^b, f_i^s and f_i^c are the body force, surface traction and concentrated force; δu_i is an arbitrary virtual displacement; ${}^{0}\Omega$ and ${}^{0}S$ represent the structural volume and surface area at time $t = 0$.

Consider a structure under two cases of static loadings with both geometrical and material nonlinearities. Let $F^{(i)}$, $u^{(i)}$, $\varepsilon^{(i)}$ and $S^{(i)}$ $(i = 1, 2)$ denote the applied loads and the nonlinear solutions for displacement, strain and stress respectively for the two load cases. These nonlinear solutions are usually obtained involving iterations and load increments via load scaling factors α_i $(i = 1, 2)$ varying between zero and unity. This leads to the pair of force-displacement $(\alpha_i F^{(i)} \sim u^{(i)}(\alpha_i))$ and stress-strain $(\alpha_i S^{(i)} \sim \varepsilon^{(i)}(\alpha_i))$ relationships. Fig. 2(a) and (b) illustrate schematically such curves with left superscript k denoting the results at the kth load incremental step in standard NFEA based on the total Lagrangian formulation. To calculate mutual work and mutual strain energy, we set $\alpha_2 = \alpha_1 = \alpha$ to enable crossover of the above force-displacement and stress-strain relationships, i.e., $\alpha F^{(1)} \sim u^{(2)}(\alpha)$ and $\alpha S^{(1)} \sim \varepsilon^{(2)}(\alpha)$, or $\alpha F^{(2)} \sim u^{(1)}(\alpha)$ and $\alpha S^{(2)} \sim \varepsilon^{(1)}(\alpha)$. As the load increments for load cases (1) and (2) are synchronized $(\alpha_2 = \alpha_1 = \alpha)$, one can also plot the force-displacement (e.g., $\alpha F^{(1)} \sim u^{(2)}(\alpha)$) and stress-strain (e.g., $\alpha S^{(1)} \sim \varepsilon^{(2)}(\alpha)$) curves based on the NFEA results at different load incremental steps, as shown in Fig. 2(c) and (d).

Now, by using the virtual work principle and NFEA for two loading cases, at the kth load step, one has:

$${}^{k}\boldsymbol{F}^{(1)}\delta\boldsymbol{u}^{(2)} = \int_{{}^{0}\Omega} {}^{k}S_{ij}^{(1)}\delta\varepsilon_{ij}^{(2)}d\Omega \ (k = 1, 2, \ldots, \mathrm{n}) \tag{1b}$$

$$\int_{0}^{{}^{k}u^{(2)}} \boldsymbol{F}^{(1)}d\boldsymbol{u}^{(2)} = \int_{{}^{0}\Omega}\left(\int_{0}^{{}^{k}\varepsilon_{ij}^{(2)}} S_{ij}^{(1)}d\varepsilon_{ij}^{(2)}\right)d\Omega \ (k = 1, 2, \ldots, \mathrm{n}) \tag{1c}$$

where $\boldsymbol{F}$ and $\boldsymbol{u}$ are the force and displacement vectors; k (=1,2,…,n) and n denote the kth load increment and the total number of load increments in NFEA; superscripts (1) and (2) represent the virtual and real load cases.

Consider Eq. (1c) for two adjacent loads ${}^{k\text{-}1}\alpha\boldsymbol{F}^{(i)}$ and ${}^{k}\alpha\boldsymbol{F}^{(i)}$ $(i = 1, 2)$, one can obtain:

$$\int_{u^{(2)}(\alpha)}^{u^{(2)}(\alpha+\Delta\alpha)} \boldsymbol{F}^{(1)}d\boldsymbol{u}^{(2)}(\alpha) = \int_{{}^{0}\Omega}\left(\int_{\varepsilon_{ij}^{(2)}(\alpha)}^{\varepsilon_{ij}^{(2)}(\alpha+\Delta\alpha)} S_{ij}^{(1)}(\alpha)d\varepsilon_{ij}^{(2)}(\alpha)\right)d\Omega \tag{2a}$$

$$\int_{{}^{k-1}u^{(2)}}^{{}^{k}u^{(2)}} \boldsymbol{F}^{(1)}d\boldsymbol{u}^{(2)} = \int_{{}^{0}\Omega}\left(\int_{{}^{k-1}\varepsilon_{ij}^{(2)}}^{{}^{k}\varepsilon_{ij}^{(2)}} S_{ij}^{(1)}d\varepsilon_{ij}^{(2)}\right)d\Omega \ (k = 1, 2, \ldots, n) \tag{2b}$$

As an approximation, Eq. (2b) can be written as

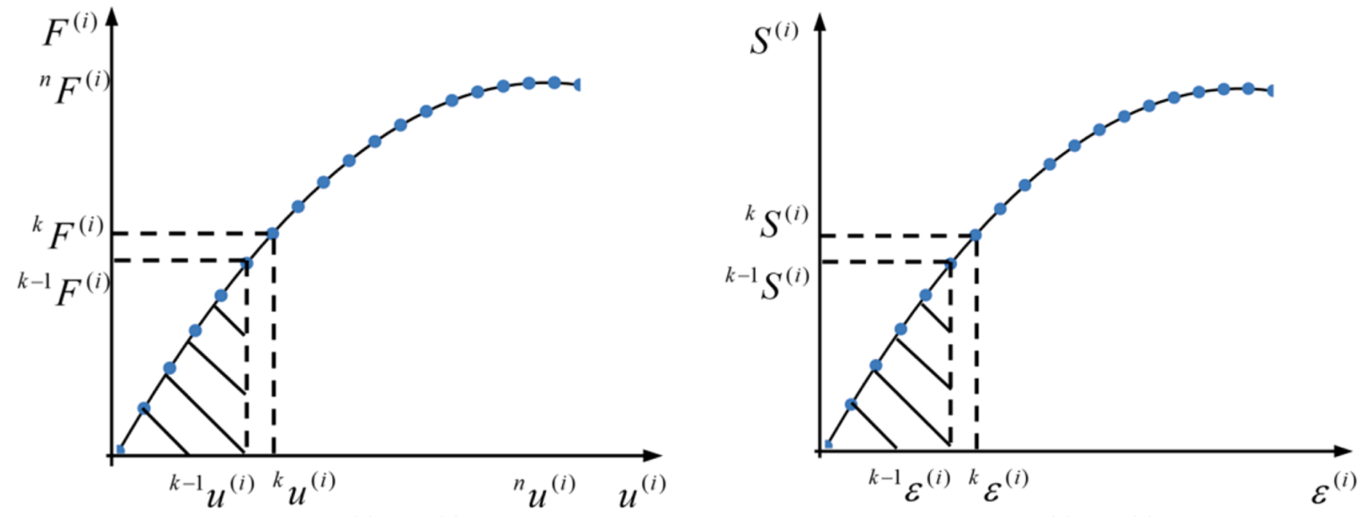

(a) $F^{(i)}\sim u^{(i)}$ (b) $S^{(i)}\sim\varepsilon^{(i)}$

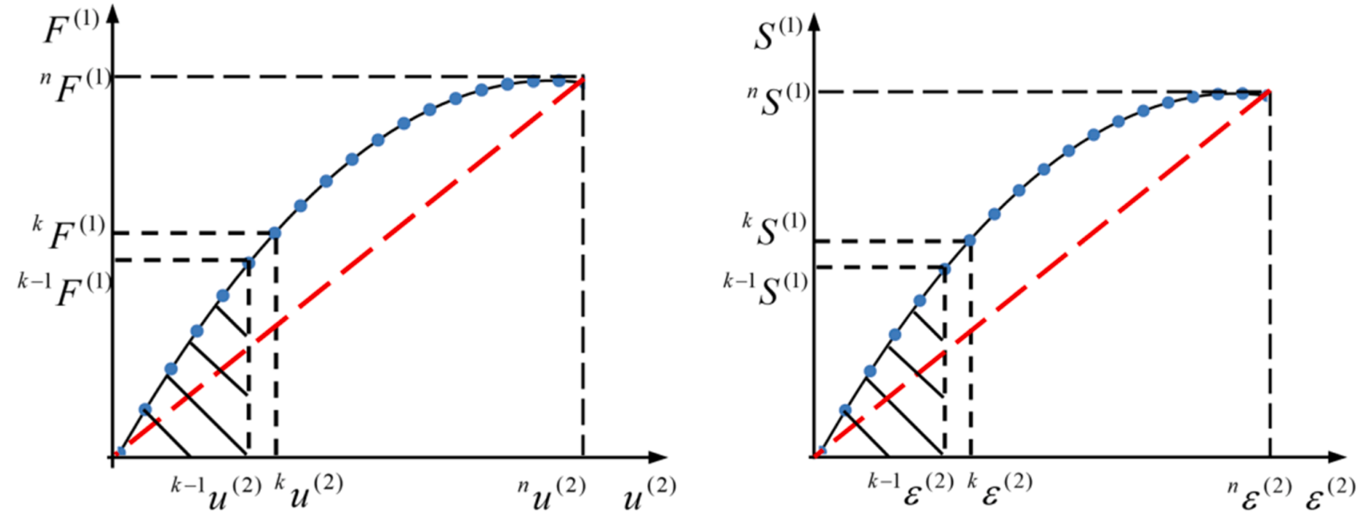

(c) $F^{(1)}\sim u^{(2)}$ (d) $S^{(1)}\sim\varepsilon^{(2)}$

Fig. 2. Nonlinear force-displacement and stress-strain relationships: (a) and (b) for virtual and real load cases; (c) relationship of virtual force-real displacement; (d) relationship of virtual stress-real strain.

$$\frac{1}{2}\left({}^{k}\boldsymbol{F}^{(1)}+{}^{k-1}\boldsymbol{F}^{(1)}\right)\left({}^{k}\boldsymbol{u}^{(2)}-{}^{k-1}\boldsymbol{u}^{(2)}\right)=\int_{{}^{0}\Omega}\frac{1}{2}\left({}^{k}S_{ij}^{(1)}+{}^{k-1}S_{ij}^{(1)}\right)\left({}^{k}\varepsilon_{ij}^{(2)}-{}^{k-1}\varepsilon_{ij}^{(2)}\right)d\Omega \tag{3}$$

where $k=1,2,\dots,n$.

If we assume that load cases 1 and 2 are virtual and real, respectively, and one virtual force is applied at one port or one degree of freedom, Eq. (3) is simplified as:

$$ {}^{k}u^{(2)}-{}^{k-1}u^{(2)}=\int_{\Omega}\left[\frac{{}^{k}S_{ij}^{(1)}+{}^{k-1}S_{ij}^{(1)}}{{}^{k}F^{(1)}+{}^{k-1}F^{(1)}}\right]\left({}^{k}\varepsilon_{ij}^{(2)}-{}^{k-1}\varepsilon_{ij}^{(2)}\right)d\Omega\;(k=1,2,\dots,n) \tag{4}$$

where ${}^{k}F^{(1)}$ is the magnitude of ${}^{k}\boldsymbol{F}^{(1)}$; and ${}^{k}u^{(2)}$ is the displacement generated by the real load ${}^{k}\boldsymbol{F}^{(2)}$at this port along the direction of ${}^{k}\boldsymbol{F}^{(1)}$.

By summing n equations in Eq. (4) and assuming that ${}^{0}u^{(2)}=0$, the displacement generated by the real force in the final state can be derived as:

$$u_{ol}^{(2)}={}^{n}u_{ol}^{(2)}=\int_{{}^{0}\Omega}\Phi_{(mse)l}^{(2)}d^{0}\Omega=\int_{{}^{0}\Omega}\sum_{k=1}^{n}\left(\frac{{}^{k}\boldsymbol{S}_{ol}^{(1)}+{}^{k-1}\boldsymbol{S}_{ol}^{(1)}}{{}^{k}\boldsymbol{F}_{ol}^{(1)}+{}^{k-1}\boldsymbol{F}_{ol}^{(1)}}\right)\left({}^{k}\boldsymbol{\varepsilon}^{(2)}-{}^{k-1}\boldsymbol{\varepsilon}^{(2)}\right)d^{0}\Omega \tag{5}$$

It is evident that Eq. (5) takes into account the NFEA results of all incremental load steps and relates the real displacement to the area under the stress-strain curve rather than the area of the triangle formed by the stress and strain at the final step as shown in Fig. 2(c) and (d). Thus, this approach enhances the accuracy of evaluating the mutual strain energy integration compared to approximation using NFEA data at the final load level [10,11], and could potentially improve the objective functions. For linear analysis, Eq. (5) degenerates to expression developed by the unit load method, as real displacement ${}^{n}u^{(2)}$ in Eq. (5) is independent on the virtual force in this case. It is worth noting that the magnitude of the virtual force should be chosen according to that of the real one in order to ensure convergence and to account for nonlinear effects.

In the optimal design of compliant mechanism with nonlinear effects to maximize the displacement of an output port, Eq. (5) will be used in the present optimization, and thus the output displacement using NFEA data at all load steps will be obtained in iteration as illustrated in Fig. 2 (c) and (d). As the objective function is rigorously computed by using the NFEA data of all increment steps as compared to that by using the NFEA data in the final state only, it is expected that numerical results are more stable and stress distributions in the optimal design is more uniform.

2.2. Problem definition

The optimal design of the multi-input-output mechanism is to maximize the total displacement ($u_{out}^{(2)}$) of output ports or to minimize $-u_{out}^{(2)}$. When force F is prescribed, minimizing compliance C (=Fu) is equivalent to minimizing displacement u; therefore, the compliance caused by real forces at input ports and that by virtual forces at output ports can be expressed in terms of the total displacement ($u_{in}^{(2)}$) of input ports and that ($u_{out}^{(1)}$) of output ports. It is assumed that port numbers of the output, input and displacement constraint are N_o, N_{in} and N_c. The displacement constraint may be defined as $u_c \le u_c^*$ where u_c^* is the specified value at port c.

Topology optimization for MIMO compliant mechanisms with nonlinear effects and displacement constraints considering compliances can be stated as to find $\boldsymbol{x}_e$ so that: $min: \quad J = -u_{out}^{(2)} + u_{in}^{(2)} + u_{out}^{(1)}$ (6a)

$$s.t.: \begin{cases} {}^n\boldsymbol{R}^{(2)}(\boldsymbol{u}, \boldsymbol{x}_e) = 0 & & \lambda_1^{(2)} \ge 1 \\ {}^n\boldsymbol{R}_l^{(1)}(\boldsymbol{u}, \boldsymbol{x}_e) = 0 & (l = 1, 2, \ldots, N_o) & \lambda_{l1}^{(1)} \ge 1 \\ {}^n\boldsymbol{R}_m^{(2)}(\boldsymbol{u}, \boldsymbol{x}_e) = 0 & (m = 1, 2, \ldots, N_{in}) & \lambda_{m1}^{(2)} \ge 1 \\ {}^n u_c \le u_c^* & (c = 1, 2, \ldots, N_c) & \\ \sum_{e=1}^{N_s} (x_e V_e) \le V_f V; & 0 \le x_e \le 1 & \end{cases} \tag{6b}$$

where $\boldsymbol{x}_e$ is the design variable; N_e is the total element number; $\boldsymbol{u}$ denotes the field satisfied with the state equation; ${}^n\boldsymbol{R}$ is the residual force in a final equilibrium state; V_e, V_f, V and are the element volume, the prescribed volume fraction and total volume; subscripts l, m and c denote the input, output and constraint ports; $\lambda_1^{(2)}$, $\lambda_{l1}^{(1)}$ and $\lambda_{m1}^{(2)}$ are the buckling factors of mode 1 for the real load case $\boldsymbol{F}^{(2)}$, virtual force $\boldsymbol{F}_l^{(1)}$ and real force $\boldsymbol{F}_m^{(2)}$. In NFEA, the selection of the virtual force requires careful consideration. It should be sufficiently large to induce significant deformations in the structure but not so large that it causes the NFEA to diverge. In Eq. (6), the buckling factors are used as the constraints so that high load level generating large deformations can be applied and the convergent results can be obtained in the NFEA [48]. It should also be noted that considering buckling behavior in topology optimization with finite deformation effects is essential, and nonlinear topology optimization can also improve buckling resistance to some extent [49].

In the objective function of Eq. (6a), $u_{out}^{(2)}$, $u_{in}^{(2)}$ and $u_{out}^{(1)}$ can be expressed in the following linear combinations:

$$u_{out}^{(2)} = \sum_{l=1}^{N_o} \alpha_l {}^n u_l^{(2)} \tag{7}$$

$$u_{in}^{(2)} = \sum_{m=1}^{N_{in}} \beta_m {}^n u_m^{(2)} \tag{8}$$

$$u_{out}^{(1)} = \sum_{l=1}^{N_o} \gamma_l {}^n u_l^{(1)} \tag{9}$$

where α_l, β_m and γ_l ($m = 1, 2, N_{in}$; $l = 1, 2, N_o$) are the coefficients; when the coefficients are equal to 1, total values of the displacements ($u_{out}^{(2)}$ and $u_{in}^{(2)}$) in output and input ports caused by real load and that ($u_{out}^{(1)}$) in output ports caused by virtual forces are obtained.${}^n u_l^{(2)}$, $u_m^{(2)}$ and ${}^n u_l^{(1)}$ are calculated on the basis of Eq. (5) and can be expressed as:

$${}^n u_l^{(2)} = \int_\Omega \left[\sum_{k=1}^{n} \left(\frac{{}^k S_{lij}^{(1)} + {}^{k-1} S_{lij}^{(1)}}{{}^k F_l^{(1)} + {}^{k-1} F_l^{(1)}} \right) \left({}^k \varepsilon_{ij}^{(2)} - {}^{k-1} \varepsilon_{ij}^{(2)} \right) \right] d\Omega = \int_\Omega \Phi_{(me)l}^{(2)} d\Omega \tag{10}$$

$${}^n u_r^{(s)} = \int_\Omega \left[\sum_{k=1}^{n} \left(\frac{{}^k S_{mij}^{(s)} + {}^{k-1} S_{mij}^{(s)}}{{}^k F_r^{(s)} + {}^{k-1} F_r^{(s)}} \right) \left({}^k \varepsilon_{rij}^{(s)} - {}^{k-1} \varepsilon_{rij}^{(s)} \right) \right] d\Omega = \int_\Omega \Phi_{(se)r}^{(s)} d\Omega \tag{11}$$

where $r = l$, m and $s = 1, 2$; subscript (me) and (se) represent the mutual strain energy and the strain energy; Φ denotes the response function; In Eq. (6b), $u_c^n \le u_c^*$ denotes the displacement constraint at observation port c; u_c^* is the specified displacement.

The objective function including the mean compliances caused by real and virtual forces for compliant mechanism was studied in [6,7] and optimization for MIMO compliant mechanism was discussed in [7]. In these investigations, nonlinear effects and displacement constraints were not taken into account. In the present study, nonlinear effects and displacement constraints are considered. The present objective function is expressed in terms of generalized displacements representing the mutual strain energy and the strain energies. It can be seen from Eq. (11) that the mean compliances for both virtual and real loads are included. Therefore, artificial springs are unnecessary in optimization, and hinge-free design may be obtained.

3. Algorithm and implementation

In order to solve Eq. (6), an algorithm should have capacities to deal with load histories and low-density elements. When nonlinear effects are considered in optimization for MIMO compliant mechanism, topology highly depends on load level and numerical instability caused by low-density elements may result in iterative divergence [19,26–28,50]. A powerful nonlinear solver is also critical as the NFEA is a highly nonlinear problem normally [28,51]. In this paper, an algorithm based on the MIST [37] will be developed; the NFEA is implemented using commercial software NASTRAN. In the present algorithm, the 1st buckling factor is used to determine the load level as in [48], and the instability is eradicated by removing void elements in NFEA [28].

3.1. MIST algorithm for MIMO compliant mechanism with multi-constraints

The objective function in Eq. (6a) can be rewritten as [37]:

$$L = J + \sum_{c=1}^{N_c} \eta_c \left({}^n u_c - u_c^* \right) = \int_\Omega \Phi(\boldsymbol{u}, \boldsymbol{x}_e) H(\Phi(\boldsymbol{u}, \boldsymbol{x}_e), t_k) d\Omega + \sum_{c=1}^{N_c} \eta_c \overline{w}_c {}^n u_c^{(2)}(\boldsymbol{u}, \boldsymbol{x}_e) \tag{12}$$

where t_k is the threshold level of the Φ function for the prescribed volume fraction at the k^{th} iteration and H is the Heaviside function: $H = 1 \Leftrightarrow \Phi \ge t_k$ and $H = 0 \Leftrightarrow \Phi < t_k$; η_c ($c = 1, 2, N_c$) are the Lagrange multipliers; $\overline{w}_c$ are the weighted coefficients [41]. Φ, ${}^n u_c^{(2)}$ and $\overline{w}_c$ can be calculated by:

$$\Phi = \sum_{l=1}^{N_o} \alpha_l \Phi_{(me)l}^{(2)} + \sum_{m=1}^{N_{in}} \beta_m \Phi_{(se)m}^{(2)} + \sum_{l=1}^{N_o} \gamma_l \Phi_{(se)l}^{(1)} \tag{13}$$

$${}^n u_c^{(2)} = \int_\Omega \left[\sum_{k=1}^{n} \left(\frac{{}^k S_{cij}^{(1)} + {}^{k-1} S_{cij}^{(1)}}{{}^k F_c^{(1)} + {}^{k-1} F_c^{(1)}} \right) \left({}^k \varepsilon_{ij}^{(2)} - {}^{k-1} \varepsilon_{ij}^{(2)} \right) \right] d\Omega = \int_\Omega \Phi_{(me)c}^{(2)} d\Omega \tag{14}$$

$$\overline{w}_c = \begin{cases} w_c\left|1 - \dfrac{u_c^*}{{}^n u_c^{(2)}}\right| & {}^n u_c^{(2)} \neq 0 \\ 0 & {}^n u_c^{(2)} = 0 \end{cases} \tag{15}$$

where w_c ($c = 1, 2, \ldots, n$) are the weighted factors, which are used to reflect the influences of each displacement constraint; and $\overline{w}_c$ is used to consider that case if ${}^n u_c^{(2)}$ is equal to zero or not, so that the computation can be implemented. In this paper, one displacement constraint is considered as in [32,52] and application to the multi-displacement constraints is to be further studied.

In Eq. (12), the Lagrange multiplier is introduced to consider the displacement constraint. Eq. (12) is equivalent to Eq. (6a) when ${}^n u_c = u_c^*$ or $\eta_c = 0$. If ${}^n u_c < u_c^*$, the constraint is satisfied; if ${}^n u_c > u_c^*$, optimization of minimizing (${}^n u_c - u_c^*$) to satisfy the displacement constraint in later iterations [32,52]. The Lagrange multiplier can be determined by the first-order KKT condition as in [32,37,52]:

$$\frac{\partial L}{\partial t} = \frac{\partial J}{\partial t} + \eta_c \frac{\partial\left(\overline{w}^n u_c^{(2)}\right)}{\partial t} = 0 \ (c = 1) \tag{16}$$

Based on Eq. (16), η_c can be found as in [32,52]. In the present computation, $\eta_c = 0$ in the initialization and is found using Eq. (16) in iteration. When η_c is determined, the objective function can be expressed as:

$$L = \int_\Omega \overline{\Phi}(\boldsymbol{u}, \boldsymbol{x}_e) H(\overline{\Phi}(\boldsymbol{u}, \boldsymbol{x}_e), t_k) d\Omega \tag{17}$$

where

$$\overline{\Phi}(\boldsymbol{u}, \boldsymbol{x_e}) = \Phi(\boldsymbol{u}, \boldsymbol{x}_e) + \eta_c \overline{w}_c \Phi^{(2)}_{(me)c}(\boldsymbol{u}, \boldsymbol{x}_e) \tag{18}$$

As the objective function in MIST is expressed in an integral form over the design domain Ω as Eq. (17), the response function is determined as the integrand Eq. (18). Hence, the response function (18) can capture the nodal structural response in relation to the objective function within Ω serving as sensitivity information for updating the topology. With the response function $\overline{\Phi}(\boldsymbol{u}, \boldsymbol{x}_e)$ derived, a MIST algorithm [37,53] can be used to solve Eq. (6). The MIST algorithm to minimize compliance of nonlinear structures was discussed in detail in [24,28] where the total Lagrange formulation based NFEA [47] was discussed.

In the present algorithm, the design domain is divided into $\Omega_1^{(k)}$ with solid and grey elements and $\Omega_1^{(k)} \backslash \Omega$ with void elements ($x_e \leq x_{min}$ =ε= 10^{-3}). For the MIMO compliant mechanism with the displacement constraint, the NFEA for each virtual and real load case is conducted in $\Omega_1^{(k)}$. The MIST algorithm consists of the following steps [28]: 1) initialization, 2) NFEA in $\Omega_1^{(k)}$, 3) construction of the Φ function, 4) determination of isosurface threshold value t_k, 5) update of design variables and 6) convergent assessment. It can be described by using 3 blocks as shown in the flowchart in the Appendix: Flowchart of the present MIST algorithm and detailed below. The major extensions compared to the MIST algorithm in [24] are: dealing with multi-objective functions, dealing with multi-constraint, and new formulation for output displacement.

3.1.1. *Block 1: design update in Ω with fixed mesh*

When the $\overline{\Phi}$function surface is constructed in the Cartesian coordinate system, coordinates *x* and *y* are the nodal locations, and coordinate *z* represents the Φ value at nodes. The $\overline{\Phi}$ values are calculated based on Eq. (18) for all load cases when element *e* in $\Omega_1^{(k)}$ and those in $\Omega_1^{(k)} \backslash \Omega$ are set to be zero. The $\overline{\Phi}$ values at nodes can be interpolated by using data at elemental centers [24,28]. In this article, stress and strain at nodes are output in the NFEA. Although the $\overline{\Phi}$ can be less than, equal to or larger than zero, the $\overline{\Phi}$ values in $\Omega_1^{(k)} \backslash \Omega$ can be set to be zero as $\sigma_{ij} \approx 0$ and $\varepsilon_{ij} \approx 0$ when ε is small [28].

When the $\overline{\Phi}$ function is constructed, it will be filtered and normalized to [−1, 1]. The isosurface threshold level t_k is determined for the prescribed volume fraction. When t_k is found, the design variables are calculated and updated as given in [24,28]. The convergence criterion is$\Delta\overline{\Phi}_k = \left[\sum_{n=1}^{N_n} \left|\overline{\Phi}_k(r_n) - \overline{\Phi}_{k-1}(r_n)\right|\right] / \left[V_f N_n\right] \leq 0.1\%$, where $\overline{\Phi}_k(r_n)$ ($k =$ 1, 2, N_n) is the value at node r_n and N_n is the total node number.

3.1.2. *Block 2: NFEA in $\Omega_1^{(k)}$*

In the NFEA in $\Omega_1^{(k)}$, the residual force equations in Eq. (6b) are solved and the stress and strain vectors at every load step are extracted, with which the mutual strain energy densities are calculated using all incremental load steps, i.e., Eq. (5), and the response function $\overline{\Phi}$ (Eq. (18) can be calculated. In the NFEA computation, the following settings are applied. When material nonlinearity is considered, sensitivity analysis for nonlinear materials needs to be iteratively found, leading to tremendous computational cost. It may be available only for simple cases [22,28,51,54,55], e.g., for bilinear elastoplastic material, the model can be: $E_e = x_e^{p_1} E$; $\sigma_e^Y = x_e^{p_2} \sigma^Y$, $E_e^T(\varepsilon) = x_e^{p_3} E^T$ where σ^Y is the yielding stress; E^T is the tangential modulus; p_1, p_2 and p_3 are the penalties. An alternative material model is to use stress-strain relationships [22,51]: $\sigma_e = x_e^p \sigma(\varepsilon)$ where σ_e denotes the stress in element *e*; $\sigma(\varepsilon)$ is the prescribed stress-strain relationships and *p* (=3) is the penalty. This material model will be used in this work.

In the present algorithm, void elements will be removed from the NFEA computation. The material can reappear in the void region via interpolating, filtering and intersecting the Φ function as indicated in Fig. 6 of [28]. As void elements are not involved in the NFEA, load path continuity in $\Omega_1^{(k)}$ is checked via a linear FEA, which is interactive with the data process block to adjust parameter ε so that the NFEA could be conducted in $\Omega_1^{(k)}$ that varies with iteration. In optimization for nonlinear structures, the optimized topology is highly dependent on load levels [56]. In the present algorithm, the load magnitude at iteration *k* is calculated by [22,48]:

$$P^k = \overline{\lambda}_1^{k-1} P^{k-1} \tag{19}$$

where $P^{k-1}$and $P^k$are the applied loads at iterations (*k*-1) and *k*; $\overline{\lambda}_1^{k-1}$ is the buckling factor of the 1st mode at iteration (*k*-1). In the present computation, the NFEA is conducted for all virtual and real load cases and the results of all load steps are used; the buckling constraint is used to determine load levels as in [48] so that nonlinear effects can be reflected in optimization and the NFEA will converge.

3.1.3. *Block 3: data process to create NFEA input file and extract the output data*

This data process block is interactive with the other two blocks to: (a) generate the input data file using the updated design variables and the initialized data where void elements will be removed when x_e is less than ε by deleting the associated material, connectivity and property definitions and the value of ε may also be adjusted to ensure the load path continuity; (b) extract the NFEA results in $\Omega_1^{(k)}$ in all load steps for each load case; and (c) transform the NFEA results in $\Omega_1^{(k)}$ to those in Ω via the established relationships of element and node numbers in Ω and in $\Omega_1^{(k)}$.

3.2. *Interface with NFEA and implementation*

Implementing procedures of the MIST algorithm were given in details in [53]; the NFEA for optimization of nonlinear structures was discussed in [28]; and the MIST algorithm for minimizing compliance with geometrical nonlinearity was detailed in [24].

In the present optimization for compliant mechanisms with geometrical and material nonlinearities, the MIST algorithm is coded in

MATLAB and interfaced with NASTRAN as the NFEA solver. The optimization is interfaced with NASTRAN via the NFEA input and output text files, which can be generated and extracted by MATLAB. Corresponding to the 3 blocks, implementation includes generating input files for the NFEA, extracting the NFEA results, and processing the data to update design variables as detailed in [24].

4. Numerical results

Numerical results are presented for single and two-output compliant mechanisms considering geometrical and material nonlinearities. Elastic constants, design domains, boundary conditions, meshes, and volume fractions of the two design problems are depicted in Fig. 3(a) and (b), which are the same as those in [12] and [6], respectively. The nonlinear properties for the single and two output mechanisms are given in Fig. 3(c) and (d). In the present computations, plane stress state is assumed.

4.1. Single-output compliant mechanism

In this section, a force inverter is studied by the present algorithm, where the compliance is not considered but artificial springs are used for comparison. The design case is to find x_e so that:

$$min: \quad u_{out} = \int_{\Omega} \left[\sum_{k=1}^{n} \left(\frac{{}^{k}\sigma_{ij}^{(1)} + {}^{k-1}\sigma_{ij}^{(1)}}{{}^{k}F_{out}^{(1)} + {}^{k-1}F_{out}^{(1)}} \right) \left({}^{k}\varepsilon_{ij}^{(2)} - {}^{k-1}\varepsilon_{ij}^{(2)} \right) \right] d\Omega \tag{20}$$

4.1.1. Linear analysis and comparison

Input data identical to those in the literature [12] are used: $F_{in} = 1$, $F_{out} = 1$; $k_{in} = 1$, and $k_{out} = 1 \times 10^{-3}$. Displacements in input (u_{in}) and output ($-u_{out}$) ports computed by the present algorithm are illustrated in Fig. 4(a), where the embedded figures are the optimized density plot (left) and topology (right); N_solid and N_void denote numbers of solid ($x_e \geq 0.999$) and void elements ($x_e \leq \varepsilon = 0.001$). It can be seen from Fig. 4(a) that void elements are effectively removed, and the removal of void elements will play a critical role in nonlinear analysis.

By comparing with numerical results in [12], the density plot in Fig. 4(a) is the same as that of Fig. 4 in [12]; the output displacement ($-u_{out} = 2.21$) correlates well with that in [12] where ($-u_{out}$) = 2.25, 2.13 and 2.55 for the sensitivity, density and close filter techniques. In the present computation, the parameters similar to those in [12] are used: filter radius $r_{min} = 0.04$; $x_{min} = 10^{-3}$; penalty $p = 1$ and then increases to 3 via '$p = p + 0.05$'. Dynamic move limit k_{mv} with an initial value of 0.3 is adopted. Fig. 4(a) validated the present algorithm for the single-output compliant mechanism in linear analysis.

Fig. 4(b) illustrates material distributions (densities) and topologies

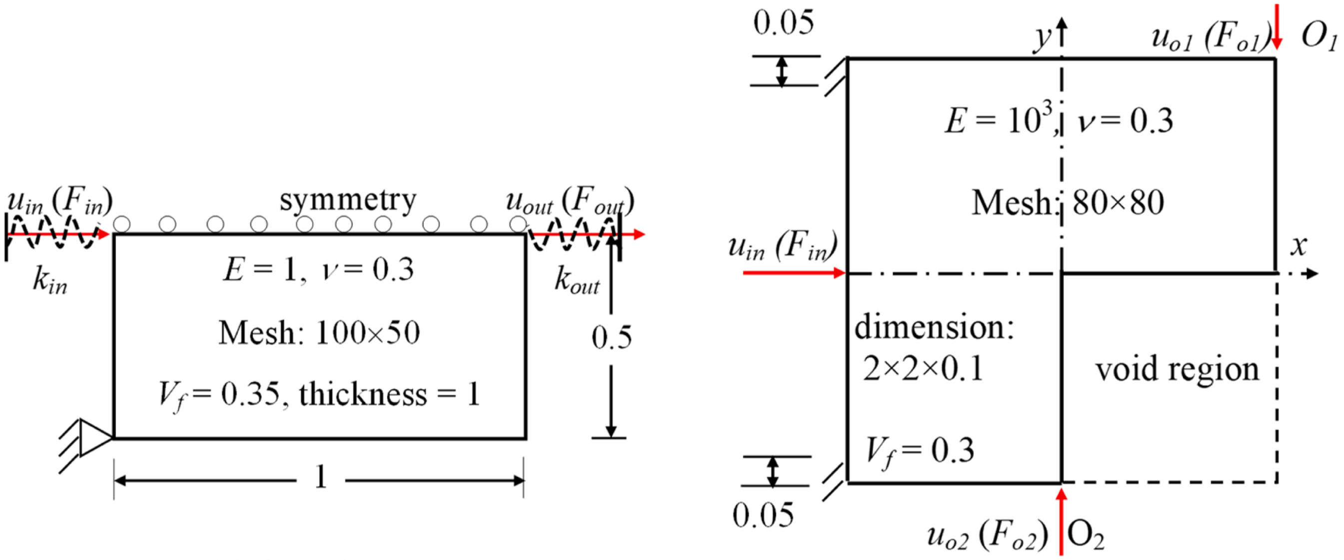

(a) force inverter

(b) two output mechanism

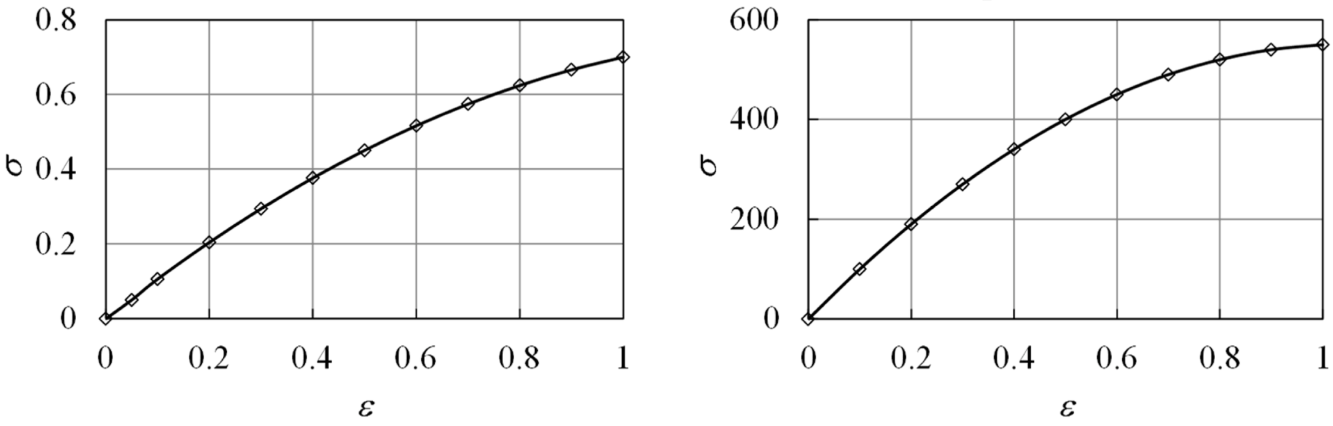

(c) stress-strain relationship for (a)

(e) stress-strain relationship for (b)

Fig. 3. Input data (a) design domain of a force inverter; (b) design domain of two output mechanism; (c) nonlinear material properties for (a); (d) nonlinear material properties for (b).

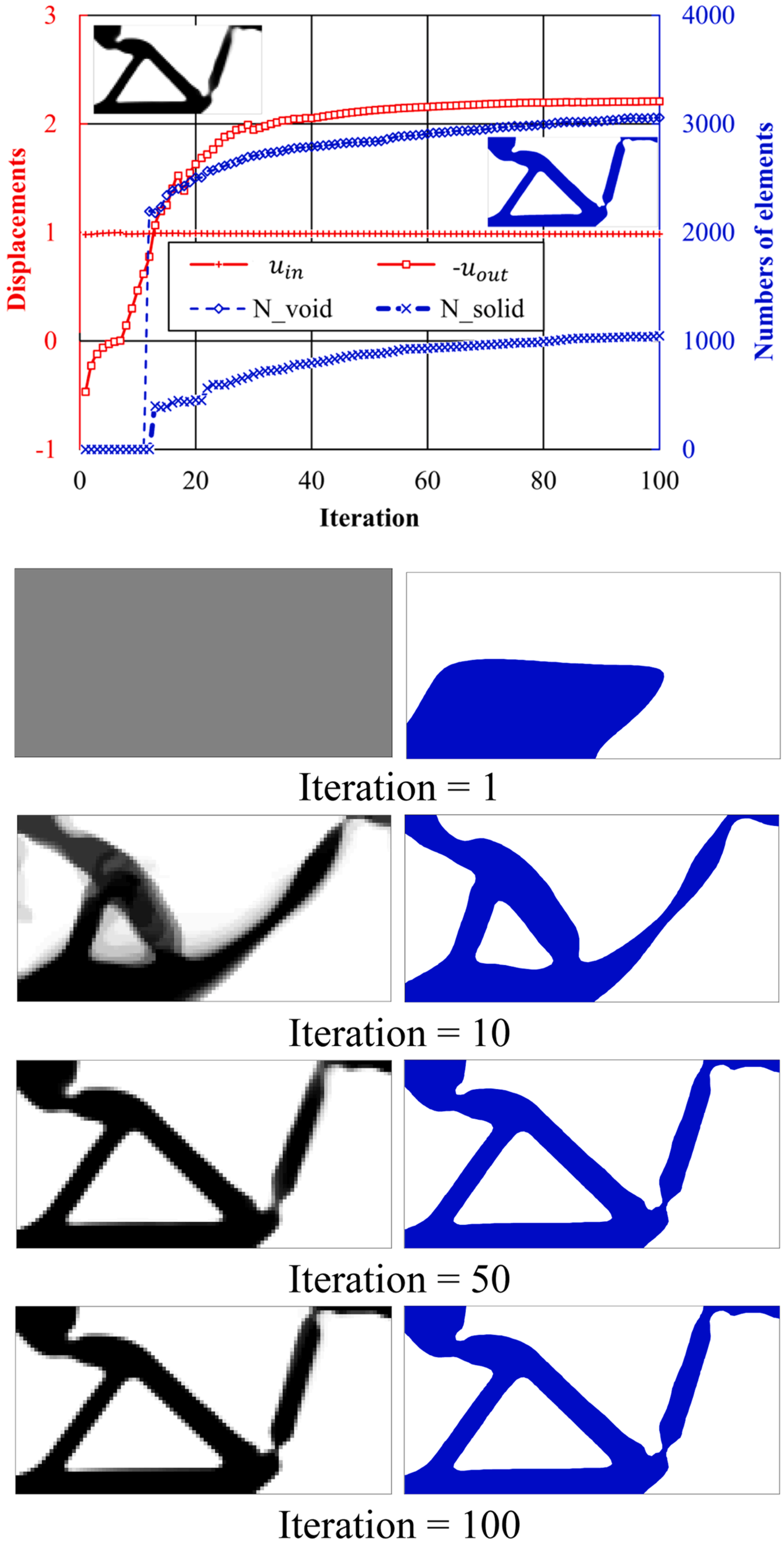

Fig. 4. (a). Output displacements versus iteration in optimization to maximize ($-u_{out}$) in linear analysis where the embedded figures are optimized density (left) and topology (right). (b). Densities (left) and topologies (right) at iterations 1, 10, 50 and 100.

at iterations 1, 10, 50 and 100. The curve in Fig. 4(a) shows that the converged value is reached after iteration 50, and Fig. 4(b) indicates that 0–1 design is obtained at iteration 50. That is, the convergence is almost achieved at iteration 50 in the present computation.

4.1.2. Optimal designs of a force inverter with nonlinear effects

In optimization for the force inverter with nonlinear effects, input data of forces and artificial springs are: F_{in}=1.0 × 10^{-2}; F_{out}=1.0 × 10^{-4}; k_{in} = 1 × 10^{-1}; and k_{out} =1 × 10^{-3}. The applied forces are determined by the buckling constraints in geometrical and material analysis and are used in other cases for comparisons. The spring stiffness in the input port is decreased to reduce its effect on nonlinear analysis, as material nonlinearity of the springs is not modeled.

Topologies and output displacements computed by using the present algorithm for 4 cases are shown in Fig. 5. The linear case, as shown in Fig. 5(a), is the same as Fig. 4 from Section 0, even though k_{in} is decreased from 1 to 1 × 10^{-1}. By comparing Fig. 5(a) with Fig. 5(b) and (c) with (d), it can be seen that the optimized densities and topologies in linear analysis and geometrically-linear but materially-nonlinear analysis are almost the same; densities and topologies in geometrically-nonlinear but materially-linear and both of nonlinear analysis using the data in a final state have minimal difference. However, there are significant differences between the designs in (a)-(b) and those in (c)-(d). It can be seen that geometrical nonlinearity has significant effects on the optimized designs, while material nonlinearity has relatively small impacts. This is consistent with results from other topology optimization methods in the literature [20,26,27], which also show that material nonlinearity plays a minor role.

(a) linear analysis $(-u_{out})$ = 0.197

(b) geometrical linear but material nonlinear analysis $(-u_{out})$ = 0.199

(c) geometrical nonlinear but material linear analysis using final state data $(-u_{out})$ = 0.153

(d) geometrical and material nonlinear analysis using data of a final state $(-u_{out})$ = 0.155

Fig. 5. Optimized densities and topologies for 4 cases: (a) linearity; (b) geometrical linearity but material nonlinearity; (c) geometrical nonlinearity but material linearity; (d) geometrical and material nonlinearity where the data in a final state are used for cases (b)-(c).

However, when stress and strain of all load steps are considered, a significantly different topology is obtained, as in Fig. 6. Fig. 6 illustrates comparisons of the optimized topologies and displacements predicted using data of all load steps and those of the final state only. It can be seen that the topology optimized using the present formulation (embedded left figure) is different from that (embedded right figure) using the final state data. The output displacement (0.171) by using the present formulation is 11 % larger than that (0.154) by using the data in a final state. Fig. 6 indicates that numerical stability by using the data of all load steps is better.

As the topologies in Fig. 6 are obtained using artificial springs, output displacements are not true values. The performance of the practical mechanisms can be studied by importing the optimized topologies into PATRAN. Fig. 7 illustrates deformations and von Mises stress distributions of the two topologies where the same enforced displacement ($u_{in} = 0.13$) is applied to the input port. Table 1 lists the output displacements of the two designs for the same applied force and the same input displacement. For the same applied force ($F_{in} = 1.29 \times 10^{-3}$) and the same input displacement ($u_{in} = 0.13$), (- u_{out}) of the design using the data of all load steps are 8.6 % and 6.4 % larger than those using the data in a final state, respectively. Table 1 also shows that the maximum force applicable in the NFEA for the design obtained by using the present formulation is much higher than that by using the final state data ($3.87 \times 10^{-3} \sim 1.59 \times 10^{-3}$). Hence, the performance of the design obtained by using the data of all load steps is clearly better.

4.2. *Multi-output compliant mechanism*

The design domain, material properties and mesh scheme for designing two-output compliant mechanism are shown in Fig. 3(b) and (d). The objective function using artificial springs or compliances is, respectively:

$$J = {}^{n}u_{o1}^{(2)} + {}^{n}u_{o2}^{(2)} \quad \text{(Using artificial springs)} \tag{21}$$

$$J = \alpha_1 u_{o1}^{(2)} + \alpha_2 u_{o2}^{(2)} + \beta_1 u_{in}^{(2)} + \gamma_1 u_{o1}^{(1)} + \gamma_2 u_{o2}^{(1)} \quad \text{(Using compliances)} \tag{22}$$

4.2.1. *Linear analysis*

By using Eq. (21), the optimized topology and density of the compliant mechanism are given in Fig. 8(a) and (c); displacement variations are plotted in Fig. 9, and output displacements are listed in Table 2, where the used parameters p and k_{mv} are the same as those in Section 4.1 and r_{min} =0.1. Artificial spring stiffness and virtual forces are: $k_{in} = 0.5$, $k_{o1} = 0.5$, $k_{o2} = 0.5$, and $F_{o1} = F_{o2} = 1$. These data are the same as those in [6], which are confirmed via private communication. In the present computation, enforced displacement u_{in}^{*} (=0.545) is applied. In addition, the enforced displacements u_{in}^{*} of 0.52 mm and 0.56 mm have also been considered in computations, resulting in almost identical topologies.

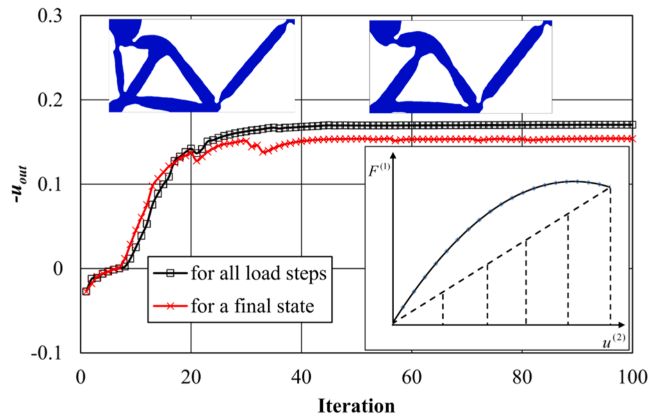

Fig. 6. Output displacements (-u_{out}) and topologies predicted by the present formulation (left topology) and using the NFEA data in a final state (right topology) in geometrical and material nonlinear analysis.

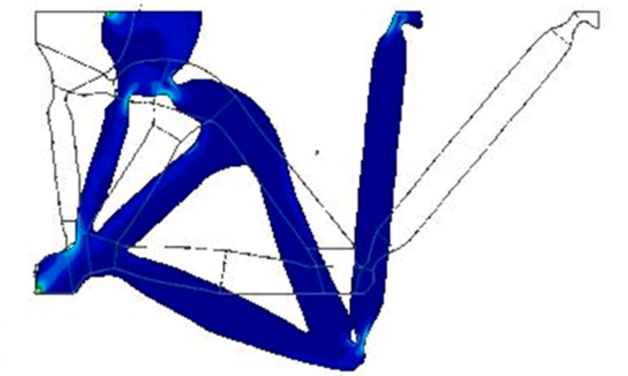

(a) optimized topology using data of all load steps

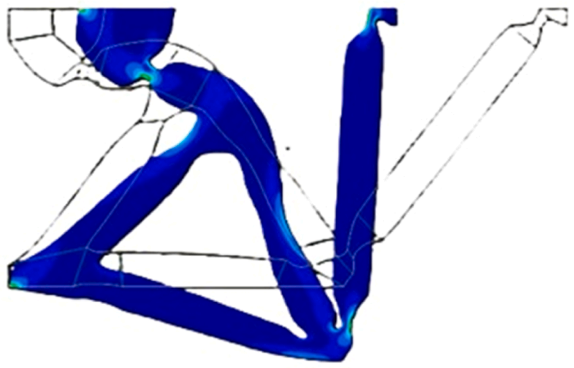

(b) optimized topology using data in a final state

Fig. 7. Deformation and von Mises stress distribution of the optimized topologies computed by using the NFEA data of (a) all load steps and (b) in a final state.

Table 1
Performance of the two optimized topologies for the same applied force or enforced input displacement.

Loadings	Method	F_{in}	u_{in}	- u_{out}
Same applied force	using data of all load steps	1.29×10^{-3}	0.131	0.354
	using data in a final state	1.29×10^{-3}	0.140	0.326
Same input displacement	using data of all load steps		0.13	0.316
	using data in a final state		0.13	0.297
The maximum force can be applied in the NFEA	using data of all load steps	3.87×10^{-3}	0.248	0.379
	using data in a final state	1.59×10^{-3}	0.180	0.343

In Fig. 9 and Table 2, $u_{o1} = u_{o1y}$, $u_{o2} = u_{o2y}$ and $u_{out} = |u_{o1y}| + |u_{o2y}|$. By comparing with the results in [6], the topology of Fig. 8(a) correlates with that of Fig. 13 in [6]. Table 2 indicates that the displacements predicted by the present algorithm are almost identical to those in [6]; the present u_{out} (=0.777) is 3.9 % larger than that (u_{out} =0.748) in [6].

In optimization for compliant mechanism, springs are conventionally attached to input and output ports. It is believed that hinges appearing in the optimized design are mainly caused by the artificial springs [6,7]. The hinge-free compliant mechanism can be obtained in topology optimization by applying minimum length scale [57] and/or stress

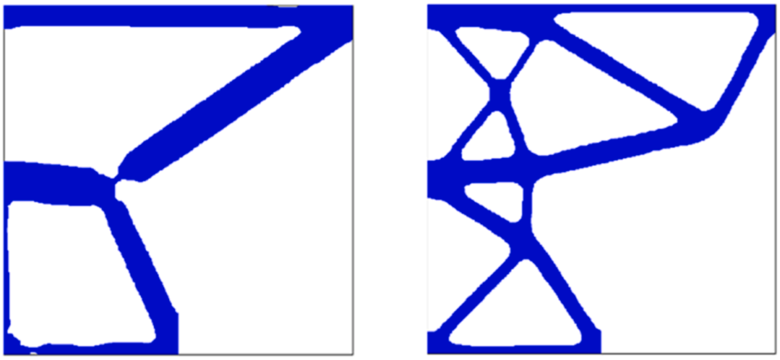

(a) topology with hinge (b) hinge-free topology

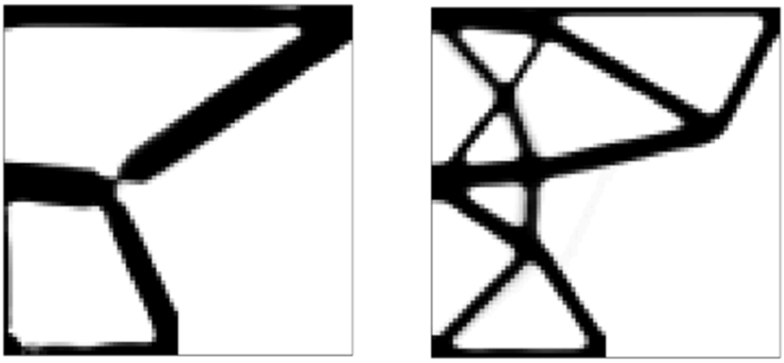

(c) density plot with hinge (d) hinge-free density plot

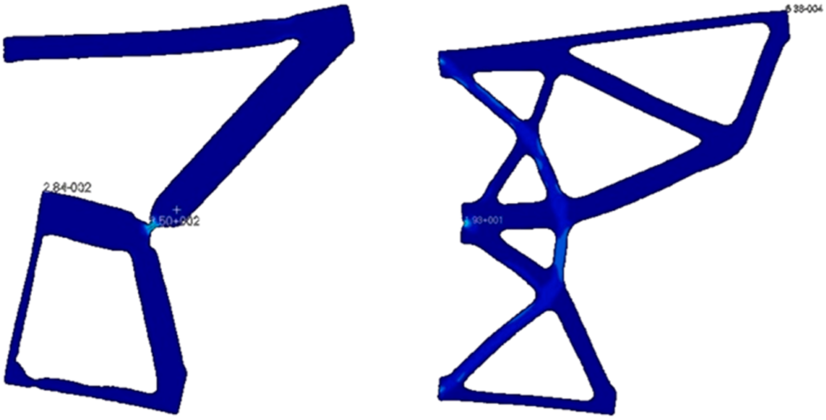

(e) deformation with von Mises stress contour for topology (a) (f) deformation with von Mises stress contour for topology (b)

Fig. 8. The topology and density obtained in linear analysis: (a) and (c) using springs; (b) and (d) using compliances. Deformation with von Mises stress distribution: (e) for topology (a); and (f) for topology (b).

constraints [30]. It can also be achieved by considering compliances [6, 7], which will be employed in this paper. When compliances are used in an objective function, it is unnecessary to use artificial springs, and both the density-based [7] and level set [6] optimization approaches can be used. In the MIST method, optimal density and topology plots can be obtained. In the present computation, an objective function in Eq. (22) is used, and the coefficients are:

$$\alpha_{11} = 1;\ \alpha_{21} = 1;\ \beta_1 = \frac{\left(\Phi^{(2)}_{(me)1} + \Phi^{(2)}_{(me)2}\right)_{\max} - \left(\Phi_{(me)1^{(2)} + \Phi^{(2)}_{(me)2}}\right)_{\min}}{\left(\Phi^{(2)}_{(se)1}\right)_{\max} - \left(\Phi^{(2)}_{(se)1}\right)_{\min}} \tag{23a}$$

$$\gamma_1 = \gamma_2 = \frac{\left(\Phi^{(2)}_{(me)1} + \Phi^{(2)}_{(me)2}\right)_{\max} - \left(\Phi^{(2)}_{(me)1} + \Phi^{(2)}_{(me)2}\right)_{\min}}{\left(\Phi^{(1)}_{(se)1} + \Phi^{(1)}_{(se)2}\right)_{\max} - \left(\Phi^{(1)}_{(se)1} + \Phi^{(1)}_{(se)2}\right)_{\min}} \tag{23b}$$

The optimized topology and density using Eqs. (22)-(23) for the enforced displacement $u_{in} = 0.05$ is illustrated in Fig. 8(b) and (d); the displacements are plotted in Fig. 10 and listed in Table 2. It can be seen that the topology of Fig. 8(b) or the density plot of Fig. 8(d) is a hinge-free design. The topology is different from that of Fig. 16 in [6], but the output displacements correlate with each other as indicated in Fig. 10 and Table 2; the present u_{out} (=0.114) is 5.8 % less than that (u_{out} =0.121) in [6]. The difference of the topologies is due to using different

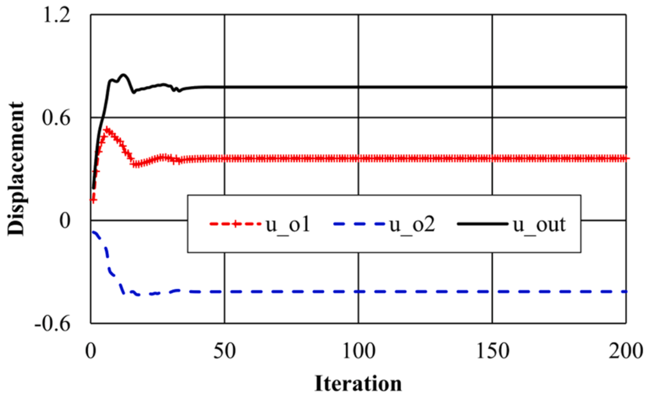

Fig. 9. Output displacement versus iteration in linear analysis without compliance component in objective function.

Table 2
Output displacements of the optimized topologies for the multi-output compliant mechanisms and comparisons.

Case	u_{in}	u_{o1}	u_{o2}	u_{out}
Fig. 8(a) (using spring)	0.545	0.362	−0.415	0.777
Zhu et al. [6] (using springs)	0.545	0.365	−0.383	0.748
Fig. 8(b) (using (compliance)	0.05	0.073	−0.041	0.114
Zhu et al. [6] (using compliances)	0.05	0.072	−0.049	0.121

compliances in the two computations. Fig. 8(e) and (f) depict von Mises stress distributions of the optimal designs by using artificial springs and compliances for the same applied force ($F_{in} = 0.0196$). The maximum von Mises in Fig. 8(e) is 350, which is considerably higher than that in Fig. 8(f). In Fig. 8(f), the maximum von stress is 4.69 in the weak region. By comparing with Fig. 16(b) in [6], von Mises stress distribution in Fig. 8(f) is more uniform. Therefore, the hinge-free design of multi-output compliant mechanism is obtained using the present optimization algorithm. This example verified the present computations for MIMO compliant mechanism in linear analysis.

4.2.2. Hinge-free designs of compliant mechanism with nonlinear effects

When Eqs. (22) and Eq. (23) are used, the optimized topologies and the output displacements predicted by the present algorithm considering geometrical and material nonlinearities are illustrated in Fig. 11. In the embedded figures, the left one is the topology obtained by using the NFEA data of all load steps, and the right one is that by using the data in a final state. The optimized topologies show that hinge-free designs are also obtained in nonlinear analysis by using the compliances without artificial springs. The enforced displacement and virtual forces for Fig. 11 are: u_{in}^{*}=0.16; F_{o1}= $\mathrm{F}_{o2} = 1 \times 10^{-2}$.

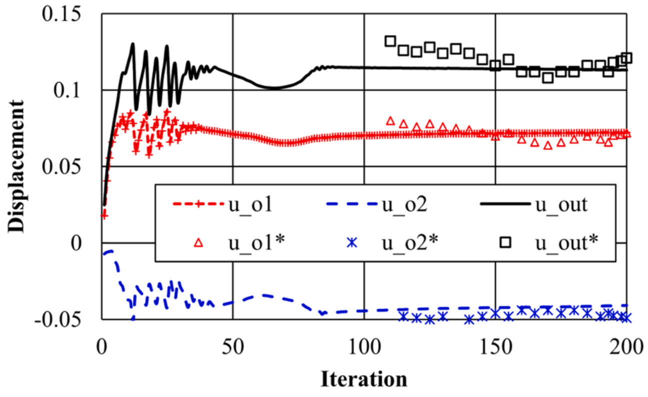

Fig. 10. Displacements computed by the present algorithm and Zhu et al. [6] (u_o1*, u_o2*, u_out*) in linear analysis using objective function with compliances caused by real and virtual forces.

Fig. 11 indicates that topologies predicted by using the data of all load steps and those in a final state are different; the output displacement (0.316) by using the present formulation is 18.8 % larger than that (0.266) by using the final state data. It is also evident that the convergence history obtained using all load step results in NFEA appears smoother and more stable than that predicted by using the final step NFEA results only. This result illustrates that the results of all load steps in NFEA should be used in the topology optimization of compliant mechanism considering geometrical and material nonlinearities.

4.3. Multi-output compliant mechanism with displacement constraint

Design domain and material properties shown in Fig. 3(b) and (d) are used to study optimization for the multi-output mechanism with the displacement constraint that u_{o2x} is constrained. When Eqs. (22) and (23) are adopted, the problem can be stated to find $\boldsymbol{x}_{\mathbf{e}}$ so that:

$$min: \quad J = \alpha_1 u_{o1}^{(2)} + \alpha_2 u_{o2y}^{(2)} + \beta_1 \left(u_{in}^{(2)}\right) + \gamma_1 u_{o1}^{(1)} + \gamma_2 u_{o2y}^{(1)} \tag{24a}$$

$$s.t.: \begin{cases} {}^{n}\mathbf{R}^{(2)}(\boldsymbol{u}, \boldsymbol{x_e}) = 0 & \lambda_1^{(2)} \geq 1 \\ {}^{n}\mathbf{R}_l^{(1)}(\boldsymbol{u}, \boldsymbol{x_e}) = 0 \quad (l = 1,\ 2) & \lambda_{l1}^{(1)} \geq 1 \\ u_{o2x} \leq u_{o2x}^{*} & \\ \sum_{e=1}^{N_s} (x_e V_e) \leq V_f V; \quad 0 \leq x_e \leq 1 & \end{cases} \tag{24b}$$

where ${}^{n}u_{o2x}^{(2)}$ denotes the displacement along x direction at port O_2 in Fig. 3(b) and the weighted factor w is given by:

$$w = \frac{\left(\Phi_{(me)1}^{(2)} + \Phi_{(me)2}^{(2)}\right)_{\max} - \left(\Phi_{(me)1}^{(2)} + \Phi_{(me)2}^{(2)}\right)_{\min}}{\left(\Phi_{(me)o2x}^{(2)}\right)_{\max} - \left(\Phi_{(me)o2x}^{(2)}\right)_{\min}} \tag{25}$$

The same coefficients as those in Sections 4.1 and 4.2 are used. In Eq. (24), optimization is to minimize the output, compliances and the error between the computed displacement ${}^{n}u_{o2x}^{(2)}$ and the specified one u_{o2x}^{*}.

4.3.1. Optimization for mechanism with the displacement constraint in linear analysis

The input data for this design case are the same as those in Section 4.2, except for those given here: real prescribed displacement $u_{in}^{*} = 0.16$, and virtual forces $F_{o1} = F_{o2} = 1$ and $F_{o2x} = 1$. Two cases are considered in the optimization with displacement constraint: u_{o2x}^{*}=

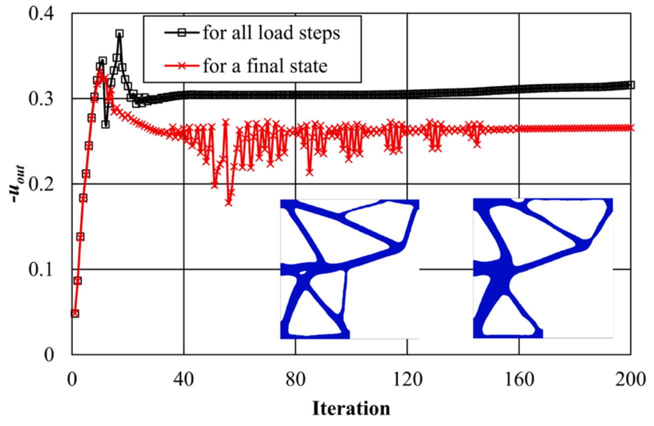

Fig. 11. Output displacements and topologies predicted by using the present formulation (left topology) and using the NFEA data in a final state (right topology).

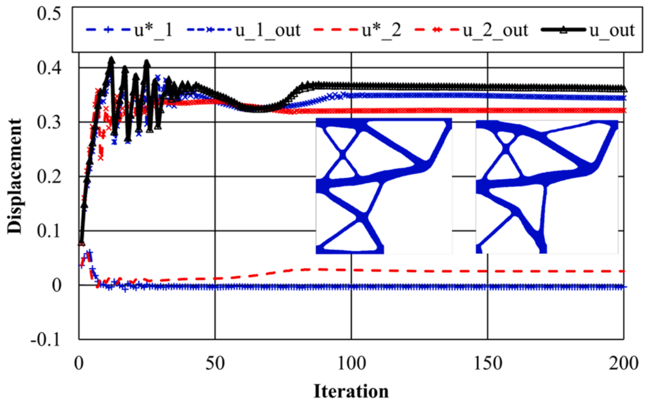

Fig. 12. Displacements and optimized designs of compliant mechanism with displacement constraints in linear analysis: left embedded figure: $\boldsymbol{u}^{*}_{o2x}$ = -0.003; right figure: $\boldsymbol{u}^{*}_{o2x}$ = 0.03.

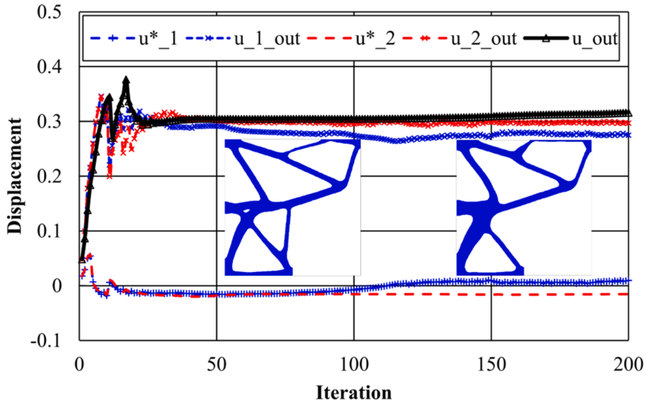

Fig. 13. Displacements and optimized topology of compliant mechanism with displacement constraints in nonlinear analysis: embedded left figure: $\boldsymbol{u}^{*}_{o2x}$ = 0.01; embedded right figure: $\boldsymbol{u}^{*}_{o2x}$ = -0.015.

−0.003 and 0.03. The output displacements for the two displacement constraint cases and the optimization without displacement constraint are illustrated in Fig. 12, where the embedded figures are the topologies for u^{*}_{o2x} = -0.003 (left) and u^{*}_{o2x} = 0.03 (right). The obtained displacements in iteration for the two cases are $u^{(2)}_{o2x}$ =−0.0034 and 0.0256, respectively.

4.3.2. *Optimal design with the displacement constraint in nonlinear analysis*

For the nonlinear case, input data are u^{*}_{in} = 0.16; F_{o1}= F_{o2} =F_{o2x} = 1 × 10^{-2}; and u^{*}_{o2x}= 0.01 and −0.015 are specified as displacement constraints, respectively, as the displacement u_{o2x} obtained when there is no displacement constraint (embedded left figure of Fig. 11) is 0.012. The optimized topologies for the two constraints are embedded in Fig. 13 where the output displacement for the optimization without displacement constraint is also plotted for comparison. The computed displacements are u^{*}_{o2x} = 0.0096 and u^{*}_{o2x} = -0.016, respectively. Figs. 12 and 13 show the effectiveness of the present algorithm in optimization for multi-output compliant mechanisms with multi-constraints. The output displacements for these cases are decreased when the displacement constraints are applied.

5. Conclusion

This study investigates multi-objective and multi-constraint topology optimization of nonlinear compliant mechanisms, considering (1) geometrical and material nonlinearities, (2) volume, displacement, and buckling constraints; and (3) hinge-free MIMO compliant mechanism designs. A novel formulation for the output displacement in terms of all load step results of NFEA of a structure is proposed, alongside an effective MIST-based method and algorithm for multi-objective and multi-constraint nonlinear topology optimization. Numerical examples for topology optimization of linear and nonlinear (geometrical and material) compliant mechanisms with one and two objectives and constraints are presented, and comparisons with the results available in the literature validate the present algorithm. The present results show that the uptake of all load step NFEA results yields a topology with larger output displacement(s) and appears more structurally stable.

The limitations of this work include: (1) the absence of explicit sensitivity analysis renders the proposed response functions, which serve as sensitivity information, less effective for multi-objective problems in updating design variables compared to those based on explicit sensitivity analysis; (2) the selection of the weighted factors w_c may require further investigation; and (3) while the proposed formulations and method are designed for MIMO optimization problems, only single-input multi-output numerical examples are presented.

CRediT authorship contribution statement

Yifu Lu: Investigation, Methodology, Writing – original draft. **Quantian Luo:** Conceptualization, Investigation, Methodology, Writing – review & editing. **Liyong Tong:** Conceptualization, Funding acquisition, Supervision, Writing – review & editing.

Declaration of competing interest

The authors declare that they have no known competing financial interests or personal relationships that could have appeared to influence the work reported in this paper.

Acknowledgements

The authors are grateful for the support of the Australian Research Council via Discovery-Project Grants DP170104916.

Appendix. : Flowchart of the present MIST algorithm

Fig. A1 illustrates the flowchart of the present MIST algorithm, which comprises three main blocks: (1) Design update in Ω with fixed mesh; (2) NFEA in $\Omega_1^{(k)}$; and (3) Data process to create NFEA input file and extract the output data. Detailed descriptions of these three blocks are provided in Section 0.

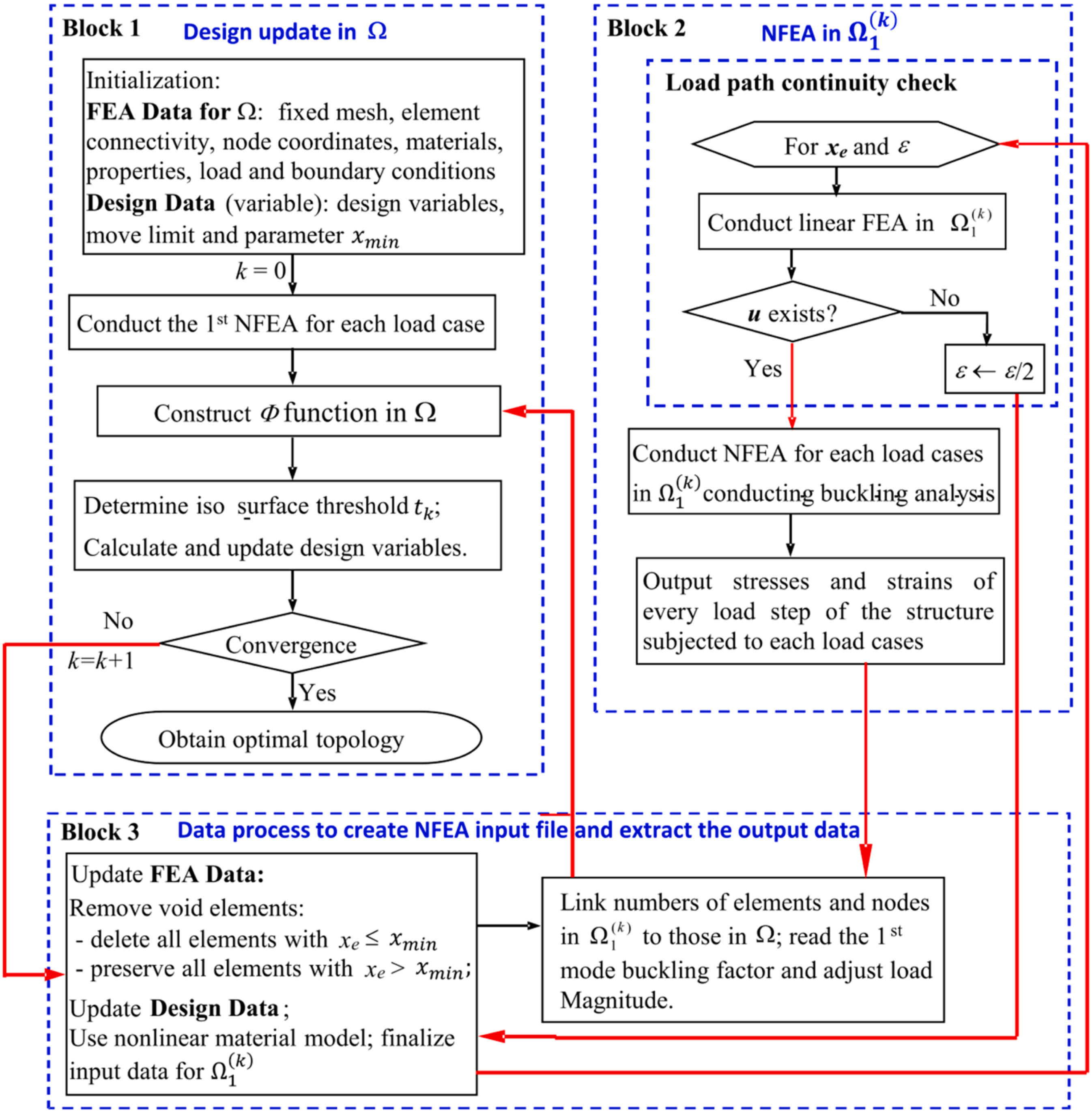

Fig. A1. Flowchart of the present MIST algorithm for topology optimization of nonlinear compliant mechanisms.

Data availability

Data will be made available on request.

References

[1] O. Sigmund, On the design of compliant mechanisms using topology optimization, Mech. Struct. Mach. 25 (1997) 493–524.

[2] R. Ansola, E. Veguería, A. Maturana, J. Canales, 3D compliant mechanisms synthesis by a finite element addition procedure, Finite Element. Anal. Des. 46 (2010) 760–769.

[3] B. Zhu, X. Zhang, S. Fatikow, N. Wang, Bi-directional evolutionary level set method for topology optimization, Eng. Opt. 47 (2015) 390–406.

[4] S. Xia, N. Wang, B. Chen, X. Zhang, W. Chen, Topology optimization of compliant mechanisms including links, supports and material distribution, Comput. Struct. 291 (2024) 107210.

[5] J. Zheng, S. Zhu, F. Soleymani, A new efficient parametric level set method based on radial basis function-finite difference for structural topology optimization, Comput. Struct. 297 (2024) 107364.

[6] B. Zhu, X. Zhang, N. Wang, Topology optimization of hinge-free compliant mechanisms with multiple outputs using level set method, Struct. Multidiscip. Optim. 47 (2013) 659–672.

[7] C. Alonso, R. Ansola, O.M. Querin, Topology synthesis of multi-input-multi-output compliant mechanisms, Adv. Eng. Softw. 76 (2014) 125–132.

[8] B. Zhu, Q. Chen, M. Jin, X. Zhang, Design of fully decoupled compliant mechanisms with multiple degrees of freedom using topology optimization, Mech. Mach. Theory 126 (2018) 413–428.

[9] J. Rong, X. Rong, L. Peng, J. Yi, Q. Zhou, A new method for optimizing the topology of hinge-free and fully decoupled compliant mechanisms with multiple inputs and multiple outputs, Int. J. Numer. Methods Eng. 122 (2021) 2863–2890.

[10] T.E. Bruns, D.A. Tortorelli, Topology optimization of non-linear elastic structures and compliant mechanisms, Comput. Meth. Appl. Mech. Eng. 190 (2001) 3443–3459.

[11] D. Jung, H.C. Gea, Compliant mechanism design with non-linear materials using topology optimization, Int. J. Mech. Mater. Des. 1 (2004) 157–171.

[12] O. Sigmund, Manufacturing tolerant topology optimization, Acta Mechanica Sinica/Lixue Xuebao 25 (2009) 227–239.

[13] E. Lee, H.C. Gea, A strain based topology optimization method for compliant mechanism design, Struct. Multidiscip. Optim. 49 (2014) 199–207.

[14] Z. Luo, L. Tong, A level set method for shape and topology optimization of large-displacement compliant mechanisms, Int. J. Numer. Methods Eng. 76 (2008) 862–892.

[15] G. Stankiewicz, C. Dev, P. Steinmann, Geometrically nonlinear design of compliant mechanisms: topology and shape optimization with stress and curvature constraints, Comput. Methods Appl. Mech. Eng. 397 (2022) 115161.

[16] D.M. De Leon, J.F. Gonçalves, C.E. de Souza, Stress-based topology optimization of compliant mechanisms design using geometrical and material nonlinearities, Struct. Multidiscip. Optim. 62 (2020) 231–248.

[17] R. Xue, C. Liu, W. Zhang, Y. Zhu, S. Tang, Z. Du, X. Guo, Explicit structural topology optimization under finite deformation via Moving Morphable Void (MMV) approach, Comput. Methods Appl. Mech. Eng. 344 (2019) 798–818.

[18] R. Kemmler, A. Lipka, E. Ramm, Large deformations and stability in topology optimization, Struct. Multidiscip. Optim. 30 (2005) 459–476.

[19] Y.S. Eom, S.Y. Han, A new topology optimization scheme for nonlinear structures, J. Mech. Sci. Technol. 28 (2014) 2779–2786.

[20] F. Wang, B.S. Lazarov, O. Sigmund, J.S. Jensen, Interpolation scheme for fictitious domain techniques and topology optimization of finite strain elastic problems, Comput. Methods Appl. Mech. Eng. 276 (2014) 453–472.

[21] T. Buhl, C.B.W. Pedersen, O. Sigmund, Stiffness design of geometrically nonlinear structures using topology optimization, Struct. Multidiscip. Optim. 19 (2000) 93–104.

[22] M.P. Bendsoe, O. Sigmund, Topology Optimization: Theory, Methods and Applications, Springer, Berlin; New York, 2003.

[23] Y. Zhao, G. Guo, W. Zuo, MATLAB implementations for 3D geometrically nonlinear topology optimization: 230-line code for SIMP method and 280-line code for MMB method, Struct. Multidiscip. Optim. 66 (2023) 146.

[24] Q. Luo, L. Tong, A deformation mechanism based material model for topology optimization of laminated composite plates and shells, Compos. Struct. 159 (2017) 246–256.

[25] W. Zuo, X. Xie, R. Zhang, Y. Lu, T. Tang, L. An, J. Bai, Geometrically nonlinear topology and fiber orientation optimization of composite structures using membrane-embedded model, Thin-Walled Struct. 203 (2024) 112250.

[26] D. Jung, H.C. Gea, Topology optimization of nonlinear structures, Finite Element. Anal. Des. 40 (2004) 1417–1427.

[27] X. Huang, Y.M. Xie, Bidirectional evolutionary topology optimization for structures with geometrical and material nonlinearities, AIAA J. 45 (2007) 308–313.

[28] Q. Luo, L. Tong, An algorithm for eradicating the effects of void elements on structural topology optimization for nonlinear compliance, Struct. Multidiscip. Optim. 53 (2016) 695–714.

[29] B. Wang, J. Bai, S. Lu, W. Zuo, Structural topology optimization considering geometrical and load nonlinearities, Comput. Struct. 289 (2023) 107190.

[30] D.M. De Leon, J. Alexandersen, J.S.O. Fonseca, O. Sigmund, Stress-constrained topology optimization for compliant mechanism design, Struct. Multidiscip. Optim. 52 (2015) 929–943.

[31] G.A. da Silva, A.T. Beck, O. Sigmund, Topology optimization of compliant mechanisms considering stress constraints, manufacturing uncertainty and geometric nonlinearity, Comput. Methods Appl. Mech. Eng. 365 (2020) 112972.

[32] X. Huang, Y.M. Xie, Evolutionary topology optimization of continuum structures with an additional displacement constraint, Struct. Multidiscip. Optim. 40 (2010) 409–416.

[33] Z.H. Zuo, Y.M. Xie, Evolutionary topology optimization of continuum structures with a global displacement control, CAD Comput. Aided Des. 56 (2014) 58–67.

[34] X. Rong, J. Zheng, C. Jiang, Topology optimization for structures with bi-modulus material properties considering displacement constraints, Comput. Struct. 276 (2023) 106952.

[35] Z. Liu, J.G. Korvink, Using artificial reaction force to design compliant mechanism with multiple equality displacement constraints, Finite Element. Anal. Des. 45 (2009) 555–568.

[36] L.L. Howell, Compliant Mechanisms, John Wiley & Sons, 2001.

[37] L.Y. Tong, J.Z. Lin, Structural topology optimization with implicit design variable-optimality and algorithm, Finite Element. Anal. Des. 47 (2011) 922–932.

[38] Y. Lu, L. Tong, Concurrent topology optimization of cellular structures and anisotropic materials, Comput. Struct. 255 (2021) 106624.

[39] W. Chen, L. Tong, S. Liu, Concurrent topology design of structure and material using a two-scale topology optimization, Comput. Struct. 178 (2017) 119–128.

[40] S. Vasista, L. Tong, Design and testing of pressurized cellular planar morphing structures, AIAA J. 50 (2012) 1328–1338.

[41] Q. Luo, L. Tong, Design and testing for shape control of piezoelectric structures using topology optimization, Eng. Struct. 97 (2015) 90–104.

[42] Q. Luo, L. Tong, Optimal Designs for vibrating structures using a moving isosurface threshold method with experimental study, J. Vib. Acoust. 137 (2015).

[43] Y. Lu, L. Tong, Concurrent multiscale topology optimization of metamaterials for mechanical cloak, Comput. Methods Appl. Mech. Eng. 409 (2023) 115966.

[44] W. Chen, X. Su, S. Liu, Algorithms of isogeometric analysis for MIST-based structural topology optimization in MATLAB, Struct. Multidiscip. Optim. 67 (2024) 43.

[45] M. Alfouneh, B. Keshtegar, STO-DAMV: sequential topology optimization and dynamical accelerated mean value for reliability-based topology optimization of continuous structures, Comput. Methods Appl. Mech. Eng. 417 (2023) 116429.

[46] M.I. Frecker, G.K. Ananthasuresh, S. Nishiwaki, N. Kikuchi, S. Kota, Topological synthesis of compliant mechanisms using multi-criteria optimization, J. Mech. Des. Trans. ASME 119 (1997) 238–245.

[47] K.-J. Bathe, Finite Element Procedures, Prentice Hall, Englewood Cliffs, N.J., 1996, p. c1996.

[48] L. Tong, Q. Luo, Elimination of void element influence on optimization for nonlinear compliance with a buckling constraint using moving iso-surface threshold method, in: 11th World Congress on Structural and Multidisciplinary Optimisation, Sydney Australia, 2015, pp. 1–6, 07th -12th, June 2015.

[49] Y. Guo, Z. Du, C. Liu, W. Zhang, R. Xue, Y. Guo, S. Tang, X. Guo, Explicit topology optimization of three-dimensional geometrically nonlinear structures, Acta Mechanica Sinica 39 (2023) 423084.

[50] F.A.M. Gomes, T.A. Senne, An algorithm for the topology optimization of geometrically nonlinear structures, Int. J. Numer. Methods Eng. 99 (2014) 391–409.

[51] G.H. Yoon, Y.Y. Kim, Topology optimization of material-nonlinear continuum structures by the element connectivity parameterization, Int. J. Numer. Methods Eng. 69 (2007) 2196–2218.

[52] K.A. James, J.R.R.A. Martins, An isoparametric approach to level set topology optimization using a body-fitted finite-element mesh, Comput. Struct. 90–91 (2012) 97–106.

[53] S. Vasista, L. Tong, Topology optimisation via the moving iso-surface threshold method: implementation and application, Aeronautic. J. 118 (2014) 315–342.

[54] F. van Keulen, R.T. Haftka, N.H. Kim, Review of options for structural design sensitivity analysis. Part 1: linear systems, Comput. Meth. Appl. Mech. Eng. 194 (2005) 3213–3243.

[55] R.T. Haftka, Semi-analytical static nonlinear structural sensitivity analysis, AIAA J. (1993) 31.

[56] D.W. Abueidda, S. Koric, N.A. Sobh, Topology optimization of 2D structures with nonlinearities using deep learning, Comput. Struct. 237 (2020) 106283.

[57] M. Zhou, B.S. Lazarov, F. Wang, O. Sigmund, Minimum length scale in topology optimization by geometric constraints, Comput. Meth. Appl. Mech. Eng. 293 (2015) 266–282.